Mathematical and computational modelling of skin biophysics – A review.

Georges Limbert [a, b] (g.limbert@soton.ac.uk)

[a] national Centre for Advanced Tribology at Southampton (nCATS) | Bioengineering Science Research Group, Faculty of Engineering and the Environment, University of Southampton, Southampton SO17 1BJ, United Kingdom
[b] Biomechanics and Mechanobiology Laboratory, Biomedical Engineering Division, Department of Human Biology, Faculty of Health Sciences, University of Cape Town, Anzio Road, Observatory 7925, South Africa

Abstract

The objective of this paper is to provide *a* review on some aspects of the mathematical and computational modelling of skin biophysics, with special focus on constitutive theories based on non-linear continuum mechanics from elasticity, through anelasticity, including growth, to thermoelasticity. Microstructural and phenomenological approaches combining imaging techniques are also discussed. Finally, recent research applications on skin wrinkles will be presented to highlight the potential of physics-based modelling of skin in tackling global challenges such as ageing of the population and the associated skin degradation, diseases and traumas.

Keywords: skin, biological soft tissue, biophysics, modelling, finite element, microstructure, continuum mechanics, elasticity, viscoelasticity, plasticity, growth, thermoelasticity, damage, contact, tribology, homogenisation, multiscale, *stratum corneum*, epidermis, dermis, hypodermis, surface instability, wrinkle.

Electronic Supplementary Material

Mathematical and computational modelling of skin biophysics – A review. (2017) Georges Limbert
Philosophical Transactions of the Royal Society of London Part A
Accepted for publication on June 6 2017 (invited review)

1. SUPPLEMENTARY MATERIAL

1.1 Remark about elasticity tensors in the context of finite element numerical procedures

Elasticity tensors that characterise the stiffness of a hyperelastic material can be defined in the Lagrangian and Eulerian configurations, respectively as:

$$\mathbb{C}^{\mathbf{E}} = 2\frac{\partial \mathbf{S}}{\partial \mathbf{C}} = 4\frac{\partial^2 \psi}{\partial \mathbf{C} \otimes \partial \mathbf{C}} = \frac{\partial^2 \psi}{\partial \mathbf{E} \otimes \partial \mathbf{E}} \tag{1}$$

and

$$\mathbb{c}^{\mathbf{d}} = 4\left(\mathbf{F} \otimes \mathbf{F}^{\mathrm{T}}\right) : \frac{\partial^2 \psi}{\partial \mathbf{C} \otimes \partial \mathbf{C}} : \left(\mathbf{F}^{\mathrm{T}} \otimes \mathbf{F}\right) = \left(\mathbf{F} \otimes \mathbf{F}^{\mathrm{T}}\right) : \frac{\partial^2 \psi}{\partial \mathbf{E} \otimes \partial \mathbf{E}} : \left(\mathbf{F}^{\mathrm{T}} \otimes \mathbf{F}\right) = 4\mathbf{b} : \frac{\partial^2 \psi}{\partial \mathbf{b} \otimes \partial \mathbf{b}} : \mathbf{b} \tag{2}$$

The material, so, objective, rate of the second Piola-Kirchhoff stress tensor is expressed as:

$$\dot{\mathbf{S}} = \frac{1}{2}\mathbb{C}^{\mathbf{E}} : \dot{\mathbf{C}} = \mathbb{C}^{\mathbf{E}} : \dot{\mathbf{E}} \tag{3}$$

These elasticity tensors are generally not constant and depend on deformation [1]. They are essential in the implementation of constitutive models into non-linear implicit-based finite element codes as they are used to calculate the numerical tangent stiffness, and therefore, condition the rate of convergence of the system of non-linear algebraic equations [2]. However, an aspect which is often overlooked and/or misunderstood, is that to benefit from the theoretical quadratic rate of convergence of non-linear finite element solvers of the Newton-Raphson type, it is essential to calculate the *consistently linearised* tangent modulus, consistent with the work-conjugate strain rate-stress pair, chosen in combination with the appropriate *objective stress rate*. In the finite element software package Abaqus/Implicit (Simulia, Dassault Systèmes, Providence, RI, USA), widely used in research and development across academia, government and industry, the use of the UMAT subroutine allows the user to code displacement-based constitutive models of arbitrary complexity. In that case, explicit expression of the components of the true stress (i.e. Cauchy stress) and consistent elasticity tensors corresponding to the incremental solving procedure must be provided. As an Eulerian code, and for continuum elements, Abaqus/Implicit requires the explicit definition of the tangent tensor, $\mathbb{T}^{\mathsf{ABAQUS}}$, consistent with a Zaremba-Jaumann objective rate of Kirchhoff stress and spatial strain rate so that:

$$\overset{\nabla \mathrm{ZJ}}{\boldsymbol{\tau}} = \mathbb{T}^{\mathsf{ABAQUS}} : \mathbf{d} \tag{4}$$

The spatial strain rate $\mathbf{d}$ is defined as:

$$\mathbf{d} = \frac{1}{2}\left(\dot{\mathbf{F}}.\mathbf{F}^{-1} + \mathbf{F}^{-\mathrm{T}}.\dot{\mathbf{F}}^{\mathrm{T}}\right) = \frac{1}{2}\left(\mathbf{l} + \mathbf{l}^{\mathrm{T}}\right) \tag{5}$$

where $\mathbf{l}$ is the spatial velocity gradient while the objective Zaremba-Jaumann rate of Kirchhoff stress is defined as [1]:

$$\overset{\nabla \mathrm{ZJ}}{\boldsymbol{\tau}} = \dot{\boldsymbol{\tau}} - \mathbf{w}.\boldsymbol{\tau} + \boldsymbol{\tau}.\mathbf{w} \tag{6}$$

The rate of spin $\mathbf{w}$ is introduced as:

$$\mathbf{w} = \mathbf{l} - \mathbf{d} - = \frac{1}{2}\left(\dot{\mathbf{F}}.\mathbf{F}^{-1} - \mathbf{F}^{-\mathrm{T}}.\dot{\mathbf{F}}^{\mathrm{T}}\right) = \frac{1}{2}\left(\mathbf{l} - \mathbf{l}^{\mathrm{T}}\right) \tag{7}$$

In order to derive $\mathbb{T}^{\mathsf{ABAQUS}}$, one needs to derive the tangent tensor consistent with the Lie derivative of the Kirchhoff stress tensor which is also known as the Oldroyd objective rate of this tensor. It is obtained by pulling back the *spatial* strain rate to the *material* configuration so that the resulting stress rate is calculated in that configuration, and then pushed back to the spatial configuration:

$$\overset{\nabla \mathrm{Oldroyd}}{\boldsymbol{\tau}} = \dot{\boldsymbol{\tau}} - \mathbf{l}.\boldsymbol{\tau} + \boldsymbol{\tau}.\mathbf{l}^{\mathrm{T}} = \mathbf{F}.\left[\mathbb{C}^{\mathbf{E}} : \left(\mathbf{F}^{\mathrm{T}}.\mathbf{d}.\mathbf{F}\right)\right].\mathbf{F}^{\mathrm{T}} = \mathbb{c}^{\mathbf{d}} : \mathbf{d} = \mathbb{c}^{\mathbf{d}} : \mathbf{l} \tag{8}$$

Although the final explicit form of $\mathbb{T}^{\mathsf{ABAQUS}}$ has been previously reported in the literature [3], the detailed intermediary derivation steps were not provided, and, for sake of completeness, are given below.

Equation (8) leads to:

$$\dot{\boldsymbol{\tau}} = \mathbb{c}^{\mathbf{d}} : \mathbf{l} + \mathbf{l}.\boldsymbol{\tau} - \boldsymbol{\tau}.\mathbf{l}^{\mathrm{T}} = \mathbb{c}^{\mathbf{d}} : \mathbf{l} + \mathbf{I} \overline{\otimes} \boldsymbol{\tau} : \mathbf{l} + \boldsymbol{\tau} \underline{\otimes} \mathbf{I} : \mathbf{l} = \left(\mathbb{c}^{\mathbf{d}} + \mathbf{I} \overline{\otimes} \boldsymbol{\tau} + \boldsymbol{\tau} \underline{\otimes} \mathbf{I}\right) : \mathbf{l} \tag{9}$$

where the non-standard tensor operators $\overline{\otimes}$ and $\underline{\otimes}$ are defined as [4]:

$$\left(\bullet \overline{\otimes} \circ\right)_{ijkl} = \bullet_{ik} \circ_{jl}; \qquad \left(\bullet \underline{\otimes} \circ\right)_{ijkl} = \bullet_{il} \circ_{jk} \tag{10}$$

By injecting **Equation (9)** into **Equation (6)** one obtains the following formula for the Zaremba-Jaumann rate of Kirchhoff stress:

$$\overset{\nabla \mathrm{ZJ}}{\boldsymbol{\tau}} = \left(\mathbb{c}^{\mathbf{d}} + \mathbf{I} \overline{\otimes} \boldsymbol{\tau} + \boldsymbol{\tau} \underline{\otimes} \mathbf{I}\right) : \mathbf{l} - \mathbf{w}.\boldsymbol{\tau} + \boldsymbol{\tau}.\mathbf{w} = \left(\mathbb{c}^{\mathbf{d}} + \mathbf{I} \overline{\otimes} \boldsymbol{\tau} + \boldsymbol{\tau} \underline{\otimes} \mathbf{I}\right) : \mathbf{l} - \frac{1}{2}\left(\mathbf{l} - \mathbf{l}^{\mathrm{T}}\right).\boldsymbol{\tau} + \boldsymbol{\tau}.\frac{1}{2}\left(\mathbf{l} - \mathbf{l}^{\mathrm{T}}\right) \tag{11}$$

$$\overset{\nabla \mathrm{ZJ}}{\boldsymbol{\tau}} = \left(\mathbb{c}^{\mathbf{d}} + \mathbf{I} \overline{\otimes} \boldsymbol{\tau} + \boldsymbol{\tau} \underline{\otimes} \mathbf{I}\right) : \mathbf{l} - \frac{1}{2}\left(\mathbf{I} \overline{\otimes} \boldsymbol{\tau} : \mathbf{l} + \boldsymbol{\tau} \underline{\otimes} \mathbf{I} : \mathbf{l}\right) + \frac{1}{2}\left(\mathbf{l}^{\mathrm{T}}.\boldsymbol{\tau} + \boldsymbol{\tau}.\mathbf{l}\right) \tag{12}$$

$$\overset{\nabla \mathrm{ZJ}}{\boldsymbol{\tau}} = \left[\mathbb{c}^{\mathbf{d}} + \mathbf{I} \overline{\otimes} \boldsymbol{\tau} + \boldsymbol{\tau} \underline{\otimes} \mathbf{I} - \frac{1}{2}\left(\mathbf{I} \overline{\otimes} \boldsymbol{\tau} + \boldsymbol{\tau} \underline{\otimes} \mathbf{I}\right) + \frac{1}{2}\left(\mathbf{I} \underline{\otimes} \boldsymbol{\tau} + \boldsymbol{\tau} \overline{\otimes} \mathbf{I}\right)\right] : \mathbf{l} \tag{13}$$

After simplifications, one obtains:

$$\overset{\nabla \mathrm{ZJ}}{\boldsymbol{\tau}} = \left[\mathbb{c}^{\mathbf{d}} + \frac{1}{2}\left(\mathbf{I} \overline{\otimes} \boldsymbol{\tau} + \boldsymbol{\tau} \underline{\otimes} \mathbf{I} + \mathbf{I} \underline{\otimes} \boldsymbol{\tau} + \boldsymbol{\tau} \overline{\otimes} \mathbf{I}\right)\right] : \mathbf{l} \tag{14}$$

It follows that the correct tangent tensor to input into the Abaqus/Standard UMAT user subroutine is:

$$\mathbb{T}^{\text{ABAQUS}} = \frac{1}{J}\left[\mathbb{c}^{\mathbf{d}} + \frac{1}{2}\left(\boldsymbol{\tau} \overline{\otimes} \mathbf{I} + \mathbf{I} \overline{\otimes} \boldsymbol{\tau} + \boldsymbol{\tau} \underline{\otimes} \mathbf{I} + \mathbf{I} \underline{\otimes} \boldsymbol{\tau}\right)\right] = \frac{1}{J}\mathbb{c}^{\mathbf{d}} + \frac{1}{2}\left(\boldsymbol{\sigma} \overline{\otimes} \mathbf{I} + \mathbf{I} \overline{\otimes} \boldsymbol{\sigma} + \boldsymbol{\sigma} \underline{\otimes} \mathbf{I} + \mathbf{I} \underline{\otimes} \boldsymbol{\sigma}\right) \tag{15}$$

This formula was provided by Zöllner *et al.* [3]. In indicial notation the tangent tensor can be expressed as:

$$\mathbb{T}^{\text{ABAQUS}}_{ijkl} = \frac{1}{J}\mathbb{c}^{\mathbf{d}}_{ijkl} + \frac{1}{2}\left(\sigma_{ik}\delta_{jl} + \sigma_{jl}\delta_{ik} + \sigma_{il}\delta_{jk} + \sigma_{jk}\delta_{il}\right) \tag{16}$$

and

$$\mathbb{T}^{\text{ABAQUS}}_{ijkl} = \frac{1}{J}F_{iA}F_{jB}F_{kC}F_{lD}\mathbb{C}^{\mathbf{E}}_{ABCD} + \frac{1}{2}\left(\sigma_{ik}\delta_{jl} + \sigma_{jl}\delta_{ik} + \sigma_{il}\delta_{jk} + \sigma_{jk}\delta_{il}\right) \tag{17}$$

1.2 Fibre dispersion models

It is clear that the complex microarchitecture of the collagen network in skin cannot be accurately captured by the strong assumption of *uniform* fibre alignment, even at a local level (see **Figure 1** of the main article). A better assumption, more in line with physical observations, is to assume that, at a local level, fibres are distributed around a main orientation, $\boldsymbol{n}_0$ with a certain probability to lay within a particular range of angular deviation from that main direction (**Figure 5**). This is embodied by the notion of *fibre dispersion* which can be accounted for by means of two main modelling approaches [5]. The first one, termed the "*angular integration approach*" is due to Lanir [6] while the second approach, known as the "*generalised structure tensor*" approach is due to Gasser *et al.* [7].

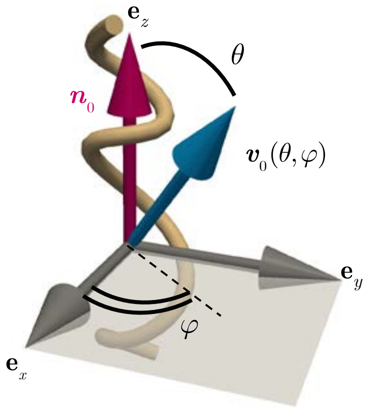

Figure 5. Schematic highlighting the Euler angles θ and φ defining the position of any vector (in that case, denoted by $\boldsymbol{v}_0$) in a three-dimensional Cartesian coordinate system defined by the unit vectors $\mathbf{e}_x$, $\mathbf{e}_y$ and $\mathbf{e}_z$. $\theta \in [0,\pi]$ and $\varphi \in [0,2\pi]$. The mean fibre direction $\boldsymbol{n}_0$ is indicated by the pink arrow aligned with the third Cartesian basis vector $\mathbf{e}_z$.

1.2.1 Angular integration approach

In this approach, also known as the *microsphere* approach, the strain energy function of a single fibre, $\psi_{fibre}(\lambda)$, is considered as a function of the fibre stretch λ. This strain energy is then integrated over the unit sphere $\mathbb{U}^2$ to represent the strain energy of a bundle of these fibres per unit reference volume, ψ_{bundle}. This could effectively be viewed as an homogenisation procedure where mesoscopic (or macroscopic) quantities are obtained by integration of fibre level microscopic quantities (e.g. strain energy of a single fibre $\psi_{fibre}(\lambda)$). It follows that:

$$\psi_{bundle} = n\int_{\mathbb{U}^2} \rho^{\boldsymbol{n}_0}(\boldsymbol{v}_0)\,\psi_{fibre}(\lambda)\,dA \tag{18}$$

where dA is the elemental solid angle, n is the number of fibres per unit reference volume, $\boldsymbol{v}_0$ is a unit vector bearing the direction of an arbitrary fibre, defined with respect to $\boldsymbol{n}_0$, a unit vector representing a mean direction around which fibre dispersion occurs, and $\rho^{\boldsymbol{n}_0}$ is the relative angular distribution of fibres around the mean direction which must satisfy the following normalisation condition [5]:

$$\frac{1}{4\pi}\int_{\mathbb{U}^2} \rho^{\boldsymbol{n}_0}(\boldsymbol{v}_0)dA = 1 \tag{19}$$

The homogenised second Piola-Kirchhoff stress tensor associated with a fibre bundle can then simply be defined as:

$$\mathbf{S}_{bundle} = 2\frac{\partial \psi_{bundle}}{\partial \mathbf{C}} = 2\,n\int_{\mathbb{U}^2} \rho^{\boldsymbol{n}_0}(\boldsymbol{v}_0)\frac{\partial \psi_{fibre}(\lambda)}{\partial \mathbf{C}}\,dA \tag{20}$$

Similarly, the associated Lagrangian elasticity tensor is:

$$\mathbb{C}^{\mathbf{E}}_{bundle} = 2\frac{\partial \mathbf{S}_{bundle}}{\partial \mathbf{C}} = 4\,n\int_{\mathbb{U}^2} \rho^{\boldsymbol{n}_0}(\boldsymbol{v}_0)\frac{\partial^2 \psi_{fibre}(\lambda)}{\partial \mathbf{C}\otimes\partial \mathbf{C}}\,dA \tag{21}$$

As pointed out by Holzapfel and Ogden [5], in **Equation (18)**, it is assumed that the elastic properties of all the fibres are defined by the same strain energy function ψ_{fibre}. This is was not the case in Lanir's study [6] where a probability distribution characterising the degree of fibre crimp, and therefore, the degree of mechanical activation, was considered, effectively leading to a modulation of ψ_{fibre} for each fibre.

1.2.2 Generalised structure tensor approach

In this ingenious approach, introduced by Gasser *et al.* [7], the idea is to use a homogenised structure tensor $\mathbf{H}$ which is obtained by integration of the structure tensor $\boldsymbol{v}_0 \otimes \boldsymbol{v}_0$ associated with an arbitrary fibre of direction $\boldsymbol{v}_0$, deviating from the mean fibre direction $\boldsymbol{n}_0$, over the unit sphere. This effectively amounts to defining a statistical strain-like invariant $(\mathbf{C} : \mathbf{H} - 1)$ (see **section 4.2.4** of the article). In that case, the strain energy of a bundle of fibres per unit reference volume ψ_{bundle} is defined as:

$$\psi_{bundle} = \psi_{bundle}(\mathbf{C}, \mathbf{H}) \tag{22}$$

where:

$$\mathbf{H} = \frac{1}{4\pi} \int_{\mathbb{U}^2} \rho^{n_0}(\boldsymbol{v}_0)\, \boldsymbol{v}_0 \otimes \boldsymbol{v}_0 \, dA \tag{23}$$

with satisfaction of the normalisation condition (19) leading to $\mathbf{H} : \mathbf{I} = 1$.

Remark

Holzapfel and Ogden [5] recently discussed important theoretical aspects of the angular integration and generalised structure tensor approaches for fibre dispersion. They demonstrated the equivalence of these two formulations in terms of predictive power and therefore, implicitly recommend the latter approach because it has been proven very effective in describing experimental data for a broad range of biological fibrous tissues, is conceptually simple, much simpler to implement in a numerical context, and also, much less demanding with regards to computational power. Moreover, and of particular significance, these authors developed a formulation based on the generalised structure tensor approach which exclude *compressed* fibres within a dispersion group. By so doing, they proved that it is indeed possible, unlike what has previously been claimed in the literature.

1.3 A common angular distribution function: the π-periodic von Mises distribution function

In his seminal paper, Lanir [6] developed a microstructurally-based plane stress model of skin in which he introduced a planar fibre angular density distribution $\mathcal{R}_k(\theta)$ where $\mathcal{R}_k(\theta)\, d\theta$ is the fraction of all fibres of type k (collagen or elastin) oriented between θ and $(\theta + d\theta)$ in the reference configuration. In that case, θ represents the deviation from the mean fibre orientation $\boldsymbol{n}_0$. Lanir selected a circular normal distribution, also known as von Mises type distribution:

$$\mathcal{R}(\theta, \mu, \kappa) = \frac{\exp(\kappa\,[\cos(\theta) - \mu])}{2\pi I_0(\kappa)} \tag{24}$$

where $I_0(\kappa)$ is the modified Bessel function of order 0. Naturally, other forms of angular distribution functions are possible [7-9]. Fibre dispersion over the unit sphere is described by a spatial density function $\rho(\theta, \varphi)$ where θ and φ represent the Eulerian angles describing the direction of any material vector $\boldsymbol{v}_0$ [7] so that one can write $\rho(\theta, \varphi) = \rho(\boldsymbol{v}_0) = \rho[\boldsymbol{v}_0(\theta, \varphi)]$ (see **Figure 5**) where:

$$\boldsymbol{v}_0(\theta, \varphi) = (\sin\theta \cos\varphi)\, \mathbf{e}_x + (\sin\theta \sin\varphi)\, \mathbf{e}_y + (\cos\theta)\, \mathbf{e}_z \tag{25}$$

$dA = \sin\theta\, d\theta\, d\varphi$ represents the infinitesimal surface area of the unit sphere defined by the angular range $[(\theta, \theta + d\theta), (\varphi, \varphi + d\varphi)]$. Without loss of generality, if one assumes that any vector $\boldsymbol{v}_0(\theta, \varphi)$ is aligned with the base vector $\mathbf{e}_z$ rotational symmetry around $\mathbf{e}_z$ is obtained and the fibre density distribution becomes independent of φ so that $\rho = \rho(\theta) = \rho[\boldsymbol{v}_0(\theta)]$. The normalisation condition is then reduced to:

$$\int_0^{\pi} \rho[\boldsymbol{v}_0(\theta)]\, dA = 2 \tag{26}$$

The dispersion of collagen fibres around a preferred mean direction (transverse isotropy) can be accounted for by the use of a modified version of the standard π-periodic von Mises distribution function with dispersion parameter b [8, 10]:

$$\rho(\theta) = 4\sqrt{\frac{b}{2\pi}}\, \frac{\exp(b\,[\cos(2\theta) + 1])}{\mathrm{erfi}(\sqrt{2b})} \tag{27}$$

where erfi is the imaginary error function defined as:

$$\mathrm{erfi}(x) = -i\frac{2}{\sqrt{\pi}}\int_0^{i\,x} \mathrm{e}^{-t^2}\,dt \tag{28}$$

It can be shown [11] that the dispersion parameter κ of the structure tensor approach of Gasser *et al.* [7] can be expressed as:

$$\kappa = \frac{1}{2} + \frac{1}{8b} - \frac{1}{4}\sqrt{\frac{2}{\pi b}}\,\frac{\exp(2b)}{\mathrm{erfi}\left(\sqrt{2b}\right)} \tag{29}$$

Instead of using a MacLaurin series expansion to approximate the imaginary error function (which is often not standard in low-level programming languages), here, it is proposed to use a global Padé decomposition established by Winitzki [12]. This approximation offers the simultaneous advantages of low computing requirement and high accuracy:

$$\mathrm{erfi}(x) \simeq \frac{\mathrm{e}^{x^2}}{x\sqrt{\pi}}\,\frac{p_n(x)}{q_n(x)} \tag{30}$$

where
$$p_n(x) = \sum_{l=1}^{n} x^{2l} \sum_{k=1}^{l} \frac{(-1)^{k-1}}{2^{n-l}}\,\frac{(2n-2l+2k-1)!!}{(2k-1)!!}\,C^n_{l-k}\,, \tag{31}$$

$$q_n(x) = \sum_{k=0}^{n} \frac{(2k-1)!!}{2^k}\,C^n_k\,x^{2n-2k} \tag{32}$$

and
$$C^n_k = \frac{n!}{(n-k)!\,k!} \tag{33}$$

The relative error between erfi and its Padé approximant can be estimated [12]:

$$\left|\frac{p_n(x)}{q_n(x)} - \mathrm{erfi}(x)\right| < 2^{-n}\sqrt{\frac{n}{2}}\left|\mathrm{erfi}(x)\right| \tag{34}$$

In a numerical context, to prevent a singularity at the origin, a small numerical parameter ε can be introduced in the approximation (30) so that:

$$\mathrm{erfi}(x) \simeq \frac{\mathrm{e}^{x^2}}{(x+\varepsilon)\sqrt{\pi}}\,\frac{p_n(x)}{q_n(x)} \tag{35}$$

The very accurate 4-term Padé approximant of the imaginary error function erfi, $\mathrm{erfi}_4^{\text{Padé}}$ is provided below:

$$\mathrm{erfi}_4^{\text{Padé}}(x) = \frac{\mathrm{e}^{x^2}}{\sqrt{\pi}}\,\frac{f(x)}{g(x)} \tag{36}$$

$$f(x) = x\left(\begin{aligned}&\frac{654729075}{512} + \frac{126351225x^2}{256} + \frac{4999995x^4}{32} + \frac{637065x^6}{16} + \frac{134805x^8}{16} + \\ &\frac{12255x^{10}}{8} + \frac{495x^{12}}{2} + 37x^{14} + \frac{11x^{16}}{2} + x^{18}\end{aligned}\right) \tag{37}$$

$$\begin{aligned} g(x) = {} & \frac{654729075}{1024} + \frac{172297125x^2}{256} + \frac{91216125x^4}{256} + \frac{2027025x^6}{16} + \frac{1091475x^8}{32} + \\ & \frac{59535x^{10}}{8} + \frac{11025x^{12}}{8} + 225x^{14} + \frac{135x^{16}}{4} + 5x^{18} + x^{20} \end{aligned} \tag{38}$$

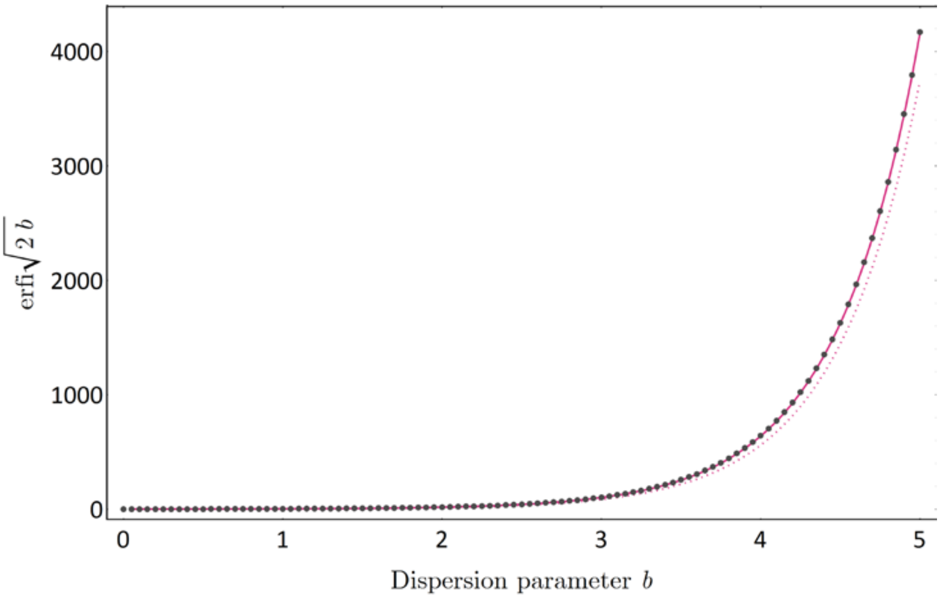

Figure 6. Comparison between $\mathrm{erfi}\sqrt{2b}$ (grey dots) and its approximation using 1 term (pink dotted line) and 4 terms (pink continuous line) in the Padé series. The 4-term series defined in **Equation (36)** shows an excellent agreement with the exact imaginary error function Erfi available in Mathematica® (Wolfram Research Inc., Champaign, IL, USA) to a nearly arbitrary order of precision.

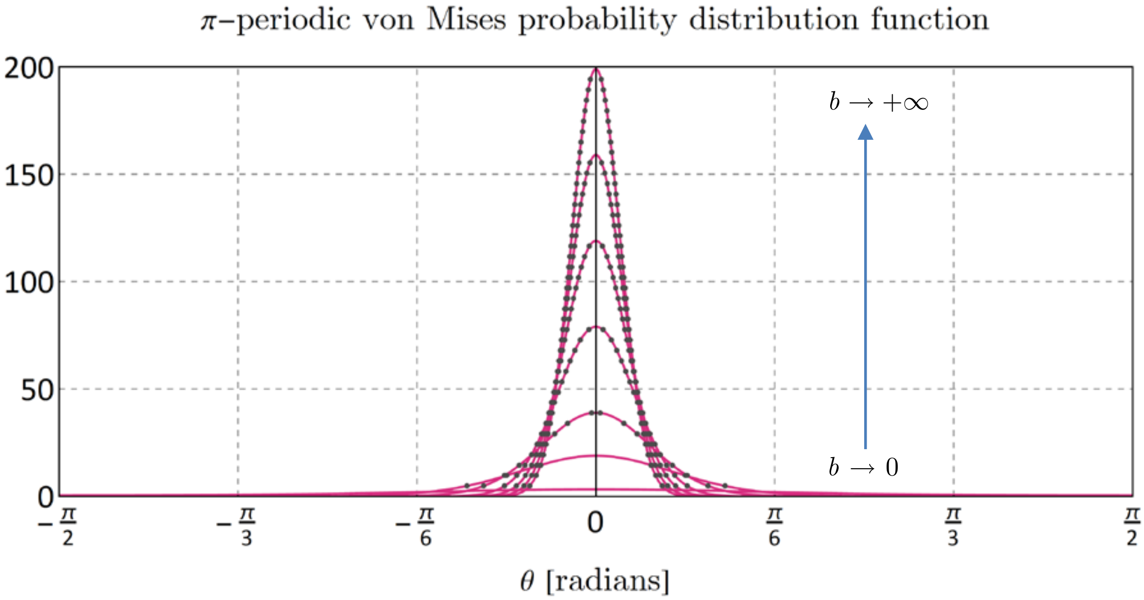

Figure 7. π-periodic von Mises angular distribution function calculated for the following dispersion parameter values: $b = \{1,5,10,20,30,40,50\}$. The continuous pink lines represent the distribution values calculated using the 4-term Padé approximant of $\mathrm{erfi}\sqrt{2b}$ defined by **Equation (36)** while the grey dots are corresponding discrete values calculated using the exact imaginary function Erfi available in Mathematica® (Wolfram Research Inc., Champaign, IL, USA).

1.4 Network models

Chain network models such as the Arruda-Boyce eight-chain model originates from concepts borrowed from statistical mechanics, namely, entropic elasticity of macromolecules [13]. In this theory, long molecular chains are assumed to rearrange their conformation under the influence of random thermal fluctuations so that their possible geometrical configurations can only be known in a statistical sense.

Polymer chains in rubber are typically described as *uncorrelated* [14] as their conformation is reminiscent of a random walk. The term *freely jointed* chains is also used. In contrast, biopolymer chains such as collagen assemblies feature smoothly varying curvature and are therefore considered *correlated*. These chains are best described using the concept of worm-like chains of Kratky and Porod [15]. In the context of soft tissue mechanics, several authors used this approach to describe the structure and mechanics of the basic building block of collagen assemblies, the tropocollagen molecule, the so-called collagen triple-helix [14, 16-21].

Both freely-jointed and worm-like entropic chains are assumed to be made of beads connected by N rigid links of equal length d, the so-called Kuhn length [22], so that the maximum length of a chain, the contour length, is $L = Nd$. The mechanics of macromolecular polymer structures is not only governed by the mechanical properties of individual chains but also by their electromagnetic and mechanical interactions which can take the form of covalent bonds, entanglement and physical cross-links. These combined effects give rise to strong network properties which can be implicitly captured by network models such as the eight-chain model of Arruda and Boyce [23]. The central idea behind these formulations is that there exists a representative nano-/microscopic unit cell able to capture network properties. The eight-chain model assumes that the unit cell is made of eight entropic chains of equal lengths connected from the centre of the cell to each of its corners (**Figure 8**), each equipped with their own strain energy ψ_{chain}. For uncorrelated and correlated chains one can consider respectively the freely jointed chain energy [**Equation (39)**] and the worm-like chain energy [**Equation (41)**] The unit cell is further assumed to feature a solid phase conferring isotropic bulk properties through the strain energy ψ_{bulk}.

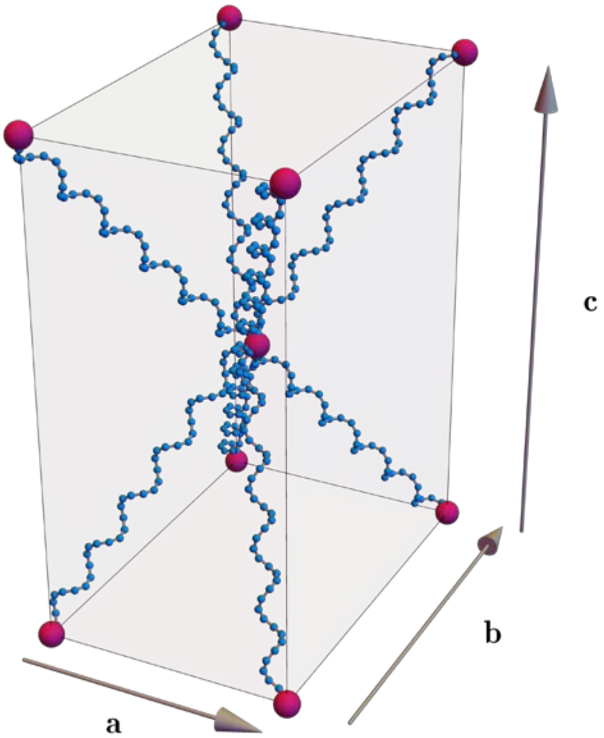

Figure 8. Schematic representation of the orthotropic eight chain network model of Bischoff *et al.* [16]. The light grey solid volume represents the bulk material admitting the strain energy function ψ_{bulk} while the eight single polymer chains are governed by the strain energy function ψ_{chain}. When $\|\mathbf{a}\| = \|\mathbf{b}\| = \|\mathbf{c}\|$ the Bischoff *et al.*'s model [16]degenerates to the Arruda-Boyce's model while the Kuhl *et al.*'s model [14] is recovered is two cell dimensions are identical (e.g. $\|\mathbf{a}\| = \|\mathbf{b}\|$).

1.4.1 The freely jointed chain model for uncorrelated chains

$$\psi_{\text{chain}} = \hat{\psi}^{FJC}_{Langevin}(r) = \hat{\psi}^{FJC}_0 + \mathfrak{K}\,\theta N \left\{ \frac{r}{L}\mathcal{L}^{-1}(r) + \ln\left[\frac{\mathcal{L}^{-1}(r)}{\sinh(\mathcal{L}^{-1}(r))} \right] \right\} \tag{39}$$

where $\hat{\psi}^{FJC}_0$ is the ground state chain energy in the unperturbed state, r the current end-to-end distance of the chain and $\mathcal{L}^{-1}$ is the inverse of the Langevin function defined as $\mathcal{L}(x) = \coth(x) - 1 / x$, $\mathfrak{K} = 1.3806503 \times 10^{-23} \left[\mathrm{m^2 kg\ s^{-2} K^{-1}} \right]$ is the Boltzmann constant and θ is the absolute temperature [K]. $\mathcal{L}^{-1}$ can be approximated using a Padé approximant [24] as:

$$\mathcal{L}^{-1}(x) \simeq \frac{3 - x^2}{1 - x^2} x \tag{40}$$

For a more in-depth analysis and alternative approximations of the inverse Langevin function, see recent papers by Nguessong *et al.* [25], Jedynak [26], Marchi and Arruda [27] and Darabi and Itskov [28].

1.4.2 The worm-like chain model for correlated chains

$$\psi_{\text{chain}} = \hat{\psi}^{WLC}(r) = \hat{\psi}^{WLC}_0 + \frac{\mathfrak{K}\,\theta L}{\Lambda} \left[2\frac{r^2}{L^2} + \frac{1}{\left(1 - \dfrac{r}{L}\right)} - 1 \right] \tag{41}$$

where L, Λ, r_0 and r are respectively the contour, persistence, initial end-to-end length and the current end-to-end length of the chain. Similarly to the freely jointed chain model, $\hat{\psi}^{WLC}_0$ is the chain energy in the unperturbed state.

1.5 Flynn-Rubin-Nielsen's formulation [29]

1.5.1 Discrete fibre vectors

The model developed by Flynn *et al.* [29] is based on a *discrete* rather than *continuous* fibre orientation distribution kernel which allows closed-form solutions for strain energy and stress. Six discrete directions are considered $\boldsymbol{n}_0^i \{i = 1,\dots,6\}$: they are oriented parallel to the lines connecting opposing vertices of a regular icosahedron (i.e. a 20-faced polyhedron). These six directions, corresponding to distinct fibre bundles, are defined as:

$$\begin{aligned}
&\boldsymbol{n}_0^1 = \frac{2}{\sqrt{5}}\mathbf{e}_1 + \frac{1}{\sqrt{5}}\mathbf{e}_3; && \boldsymbol{n}_0^2 = \frac{1}{2}\left(1 - \frac{1}{\sqrt{5}}\right)\mathbf{e}_1 + \sqrt{\frac{1}{2}\left(1 + \frac{1}{\sqrt{5}}\right)}\mathbf{e}_2 + \frac{1}{\sqrt{5}}\mathbf{e}_3 \\
&\boldsymbol{n}_0^3 = -\frac{1}{2}\left(1 + \frac{1}{\sqrt{5}}\right)\mathbf{e}_1 + \sqrt{\frac{1}{2}\left(1 - \frac{1}{\sqrt{5}}\right)}\mathbf{e}_2 + \frac{1}{\sqrt{5}}\mathbf{e}_3, && \boldsymbol{n}_0^4 = -\frac{1}{2}\left(1 + \frac{1}{\sqrt{5}}\right)\mathbf{e}_1 - \sqrt{\frac{1}{2}\left(1 - \frac{1}{\sqrt{5}}\right)}\mathbf{e}_2 + \frac{1}{\sqrt{5}}\mathbf{e}_3 \\
&\boldsymbol{n}_0^5 = \frac{1}{2}\left(1 - \frac{1}{\sqrt{5}}\right)\mathbf{e}_1 - \sqrt{\frac{1}{2}\left(1 + \frac{1}{\sqrt{5}}\right)}\mathbf{e}_2 + \frac{1}{\sqrt{5}}\mathbf{e}_3, && \boldsymbol{n}_0^6 = \mathbf{e}_3
\end{aligned} \tag{42}$$

From these six unit vectors, Flynn *et al.* [29] defined six structural tensors:

$$\mathfrak{B}_0^i = \boldsymbol{n}_0^i \otimes \boldsymbol{n}_0^i \{i = 1,\dots,6\} (\text{no summation on } i), \quad \text{with } \sum_{i=1}^{6} \mathfrak{B}_0^i = 2\mathbf{I} \tag{43}$$

1.5.2 A particular strain energy function for collagen fibre bundles assuming a unit step distribution

If one injects the definition of a unit step distribution function D:

$$D(x) = \begin{cases} 0, & x < x_1 \quad \text{or} \quad x > x_3 \\ \dfrac{1}{x_3 - x_1}, & \text{otherwise} \end{cases} \tag{44}$$

into **Equation (35)**, after simplification, one arrives to the following expression for the strain energy function of a single collagen fibre bundle:

$$\psi_c(\lambda) = \begin{cases} 0, & \lambda < x_1 \\ \dfrac{E_c}{\rho_0}\dfrac{1}{4(x_3 - x_1)}\left[(\lambda - x_1)(\lambda - 3x_1) + 2x_1^2 \ln\left(\dfrac{\lambda}{x_1}\right)\right], & x_1 \le \lambda < x_3 \\ \dfrac{E_c}{\rho_0}\left\{\dfrac{1}{4(x_3 - x_1)}\left[(x_3 - x_1)(x_3 - 3x_1) + 2x_1^2 \ln\left(\dfrac{x_3}{x_1}\right)\right] + \left(\dfrac{x_3 - x_1}{2} - x_3\right)\ln\left(\dfrac{\lambda}{x_3}\right) + \lambda - x_3\right\}, & x_3 < \lambda \end{cases} \tag{45}$$

1.6 Description of the constitutive parameters of Limbert's model [30]

Limbert's model [30] features a set of twenty three constitutive parameters $\mathbf{p} = \mathbf{p}^1 \cup \mathbf{p}^2 = \{\mathfrak{K}, \theta, \kappa, \mu_0^i, \mu_1^i, \mu_2^i, \aleph_i, L_i, L_p^i, r_i, a_i, b_i, \overline{\lambda}_i^c\}_{i=1,2}$ where:

$$\begin{aligned} \mathbf{p}^1 &= \left\{\mathfrak{K}, \theta, \kappa, \mu_0, a_{n_0}, b_{n_0}, a_{m_0}, b_{m_0}, \aleph_{n_0}, \aleph_{m_0}, \overline{\lambda}_{n_0}^c, \overline{\lambda}_{m_0}^c\right\}; \\ \mathbf{p}^2 &= \left\{\mu_1, \mu_2, L_{n_0}, L_p^{n_0}, r_{n_0}, \aleph_{m_0}, L_{m_0}, L_p^{m_0}, r_{m_0}\right\} \end{aligned} \tag{46}$$

Limbert [30] determined the parameter set $\mathbf{p}^2$ using a numerical global optimisation algorithm while the parameter set $\mathbf{p}^1$ was assumed *a priori* based on existing data [14] and data obtained via visual inspection of biaxial stress-strain curves for rabbit skin [31].

Table 1. Description of the constitutive parameters of decoupled-invariant orthotropic hyperelastic developed by Limbert [30] with assumed and numerically-optimised values obtained by identification with the rabbit skin data of Lanir and Fung [32].

	Measured or estimated constitutive parameters	
$\mathfrak{K}$	Boltzmann constant	$1.3806503.10^{-23}$ [J.K^{-1}]
θ	Absolute temperature	310 [K]
κ	Bulk modulus of the matrix	50 [kPa]
μ_0	Shear modulus of collagen fibres	0 [Pa]
a_{n_0}, a_{m_0}	First shape parameter for sigmoid coupling function (families 1 and 2)	50
b_{n_0}, b_{m_0}	Second shape parameter for sigmoid coupling function (families 1 and 2)	20
$\overline{\lambda}_{n_0}^c, \overline{\lambda}_{m_0}^c$	Critical stretch for sigmoid coupling function (families 1 and 2)	1.15 | 1.40
$\aleph_{n_0}, \aleph_{m_0}$	Density of collagen fibres (families 1 and 2)	7.10^{21} [m^{-3}]
	Constitutive parameters determined by numerical optimisation	
μ_1	Matrix shear modulus	150.123 [Pa]
μ_2	Maximum fibre-fibre/matrix-fibre shear modulus	9.981 [Pa]
L_{n_0}, L_{m_0}	Contour length of a tropocollagen molecule (families 1 and 2)	2.792
$L_p^{n_0}, L_p^{m_0}$	Persistence length of a tropocollagen molecule (families 1 and 2)	0.200 | 0.591
r_{n_0}, r_{m_0}	Initial length of a crimpled collagen molecule (families 1 and 2)	1.368 | 1.741

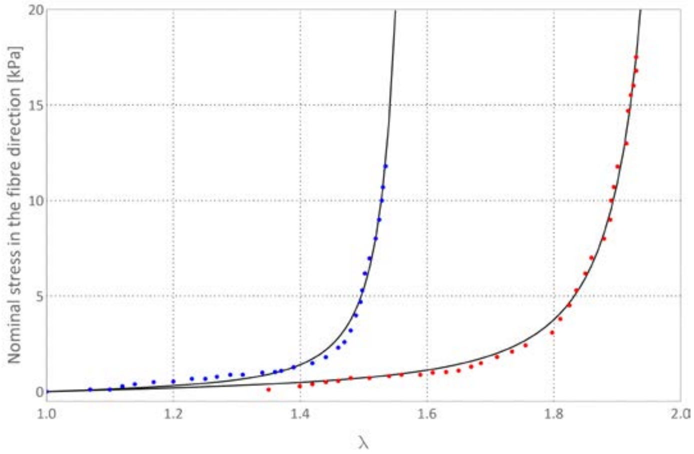

Figure 9. Experimental data from uniaxial tensile tests (stretch-nominal stress) on rabbit skin from Lanir and Fung [32] and the corresponding theoretical values (continuous lines) calculated after identification of the constitutive parameters of the decoupled invariant model developed by Limbert [30](Blue: head-to-tail fibre direction, $r^2 = 0.997$; Red: perpendicular to head-to-tail direction, $r^2 = 0.998$).

1.7 Finite strain viscoelasticity – Viscosity tensors

From the formulation established in **section 4.3.3**, the viscosity tensor for the matrix and fibre phases, denoted respectively as $\mathbb{V}_M$ and $\mathbb{V}_F$ are defined as:

$$\mathbb{V}_M^{-1} = \frac{1}{2\eta_{M_S}}\left(\mathbf{C}^v_{matrix} \odot \mathbf{C}^v_{matrix} - \frac{1}{3}\mathbf{C}^v_{matrix} \otimes \mathbf{C}^v_{matrix}\right) + \frac{1}{9\eta_{M_B}}\mathbf{C}^v_{matrix} \otimes \mathbf{C}^v_{matrix} \tag{47}$$

$$\mathbb{V}_F = \eta_{F_1}\frac{\boldsymbol{n}_0 \otimes \boldsymbol{n}_0}{\mathbf{C}^v_{fibre} : (\boldsymbol{n}_0 \otimes \boldsymbol{n}_0)} \otimes \frac{\boldsymbol{n}_0 \otimes \boldsymbol{n}_0}{\mathbf{C}^v_{fibre} : (\boldsymbol{n}_0 \otimes \boldsymbol{n}_0)} + \eta_{F_2}\frac{\boldsymbol{m}_0 \otimes \boldsymbol{m}_0}{\mathbf{C}^v_{fibre} : (\boldsymbol{m}_0 \otimes \boldsymbol{m}_0)} \otimes \frac{\boldsymbol{m}_0 \otimes \boldsymbol{m}_0}{\mathbf{C}^v_{fibre} : (\boldsymbol{m}_0 \otimes \boldsymbol{m}_0)} \tag{48}$$

where the non-standard tensor product $\odot$ is defined as:

$$(\bullet \odot \circ)_{ijkl} = (\bullet \,\overline{\otimes}\, \circ + \bullet \,\underline{\otimes}\, \circ)_{ijkl} = \frac{1}{2}(\bullet_{ik} \circ_{jl} + \bullet_{il} \circ_{jk}) \tag{49}$$

and η_{M_S} and η_{M_B} are the deviatoric and bulk viscosities of the matrix while η_{F_1} and η_{F_2} are the viscosities associated with the two families of fibres.

Particular non-equilibrium potentials for anisotropic viscoelasticity

The particular forms of the non-equilibrium viscous potentials are given as follows:

$$\Phi^v_M(J^e, \alpha^e_1) = \frac{1}{2}\kappa^v(J^e - 1)^2 + \frac{1}{2}\mu^v_M\left(\alpha^e_1 - 2\right) \tag{50}$$

$$\Phi^v_\beta(\bar{\lambda}^e_\beta) = \frac{1}{2}\mu^v_\beta\left(\bar{\lambda}^{e\,2}_\beta - 1\right)^2 \tag{51}$$

κ^v, μ^e_M, μ^v_1 and μ^v_2 are material parameters that define the properties of the elastic part of the non-equilibrium Maxwell component. This non-linear orthotropic viscohyperelastic constitutive model was implemented into a commercial finite element code and constitutive parameters were identified from proprietary experimental data.

1.8 Softening and damage

Preconditioning effects are often associated with viscoelasticity [33]. They are linked to short-term rearrangement of the tissue microstructure and, in some instances, permanent deformation and/or damage of the microstructure. Preconditioning of biological soft tissues before in vitro tensile tests is often recommended. On one hand, it is a way to re-load the tissue into a state closer to *in vivo* conditions, on the other hand, depending on the amount of pre-conditioning, this could lead to microstructural rearrangements going beyond what would be physiologically experienced by the tissue. Muñoz *et al.* [34] observed a typical softening effect—known as the Mullins effect in the context of filled rubber mechanics—during cyclic uniaxial testing of murine skin at large deformations. A similar effect was reported by Edsberg *et al.* [35] for human skin under cyclic pressures. Ehret and Itskov [36] developed a constitutive framework to capture the Mullins effects observed in biological soft tissues and fitted it to the experimental data of Muñoz *et al.* [34] demonstrating an excellent agreement.

Ehret *et al.* [37] later applied their constitutive model to porcine dermis and corroborated observations made by Muñoz *et al.*, namely the occurrence of significant residual deformations upon cycling loading. Recently, Li and Luo [38] proposed an invariant-based softening damage and failure constitutive model for human and animal skins. The 9-parameter model is based on a combination of the GOH model [7] and the energy-limiter approach of Volokh [39, 40]. The performance of the model was tested on a series of orthogonal uniaxial tensile tests on human, swine, bovine and rabbit skins and exhibited excellent results. The main drawback of the model is its conservative nature: upon unloading the material would fully recover its original shape and return to its virgin undamaged state, effectively healing. This shortcoming could easily be rectified [41].

Considering its soft interfacial and protective nature, it is reasonable to assume that, at an evolutionary level, the skin of mammals in general, and that of humans, in particular, must have evolved damage resistance strategies through optimisation of their ultrastructure.

Recently, Yang *et al.* [42] have discovered four microstructural mechanisms that explain the extreme tear resistance of rabbit skin by conducting a very comprehensive multi-modality study. This study combined physical tensile tests, scanning electron microscope, *in situ* synchrotron X-ray characterisation and constitutive modelling. The viscoelastic constitutive model used to represent the tensile response of skin is based on the mechanics of a wire made of circular segments and captures two hierarchical levels of the skin: nanometre level (collagen fibrils) and micrometer level (collagen fibres).

1.9 Plasticity

Mazza *et al.* [43, 44] developed a non-linear elasto-visco-plastic model to simulate ageing of the human face [43, 44]. It is based on the constitutive formulation of Rubin and Bodner [45] to model the dissipative response of soft tissues. In this study the dissipative effects were a combination of elastic and visco-plastic mechanisms. Rubin and Bodner [45] demonstrated the relevance of their model by capturing very well the cyclic dissipative response of superficial musculoaponeurotic system tissue. The constitutive equations were implemented as a user subroutine in the commercial finite element code Abaqus (Simulia, Dassault Systèmes, Providence, RI, USA) to simulate gravimetric descent of facial tissue [43]. Mazza *et al.* [43, 44] extended the model of Rubin and Bodner [45] by including an ageing parameter equipped with its own time evolution equation. This ageing-driven parameter was a modulator of tissue. A four-layer model of facial skin combined with a face-like geometrical base was developed and highlighted the great potential of this kind of computational models to study the effects of skin ageing on facial appearance. The Rubin and Bodner's constitutive model [45] was generalised by Weickenmeier and Jabareen [46] in terms of the viscoplasticity equations and hardening parameter whilst establishing a robust finite element framework featuring a strongly objective integration scheme. In this paper, this modelling framework was applied to identify the mechanical properties of facial skin by combining suction measurements obtained via a Cutometer® MPA 580 (Courage and Khazaka Electronic GmbH, Köln, Germany) and inverse finite element techniques. The procedure is described in more details in a subsequent paper by Weickenmeier *et al.* [47].

1.10 Growth

As any biological soft tissue, the skin undergoes growth and remodelling in physiological and abnormal conditions. This starts from morphogenesis of the embryo and continues through life as the skin ages and adapts in response to various types of physiological and abnormal physical stimulations. Examples include stretching of the skin during pregnancy and natural growth, healing and scarring in response to injury, tanning and extrinsic ageing in response to the photo-chemical effects of solar radiations, stiffening of the dermal collagen network as the result of glycation associated with diabetes.

In his seminal review paper, Taber [48] defined growth as the process of adding mass while remodelling "*involves changes in material properties*" and morphogenesis "*is the generation of animal form*". Epstein [49] recently refined these definitions by demonstrating that, given an arbitrary time-dependent constitutive law, one can establish a canonical decomposition into growth, remodelling, ageing and morphogenesis parts.

Motivated by surgical tissue expansion procedures [50], Socci *et al.* [51] developed an axisymmetric computational model of skin growth. The constitutive model was based on a multiplicative decomposition of the deformation gradient using three distinct configurations: (1) the stress-free configuration before growth; (2) the configuration at the end of the growth process, not necessarily geometrically compatible, as grown stress-free configuration; (3) the configuration of the grown body after restoring strain compatibility via elastic deformations and 4) the configuration of the grown body after subsequent application of external loads. The general point of departure of growth theories consists in multiplicatively splitting the deformation gradient $\mathbf{F} = \mathbf{F}^e.\mathbf{F}^g$ into a growth part (inelastic) $\mathbf{F}^g$ and an elastic deformation gradient $\mathbf{F}^e$ [52].

This effectively assumes that there exists an intermediate virtual configuration between the reference and current configurations in which individual *material particles* have their volume changed.

However, the growth (positive or negative) of each material particle renders them geometrically incompatible with their neighbours [48, 53]. The elastic deformations characterised by $\mathbf{F}^e$ bring back compatibility and, by so doing, introduce residual stress [54].

In the context of skin expansion procedures for reconstructive surgery, Tepole *et al.* [55] formulated a 3D constitutive model for skin growth embedded into a rigorous theoretical framework based on the thermodynamics of open systems [56]. The essence of this theory is encapsulated by the equivalence between the rate of variation of the material density ρ_0 and the mass in- and out-fluxes $\nabla_{\mathbf{X}}.\mathbf{R}$ and mass sources/sinks R_0 :

$$\frac{d\rho_0}{dt} = \nabla_{\mathbf{X}}.\mathbf{R} + R_0 \tag{52}$$

To replicate the clinically observed supra-physiological skin growth induced by balloon expansion, Tepole *et al.* [55] considered in-plane skin growth driven by a strain-based stimulus: growth occurs when a critical in-plane stretch is reached. The growth factor was described by a temporal evolution equation and the skin was modelled as a homogeneous neo-Hookean material. 3D tissue expansions were simulated by considering a series of expanders with different shapes and showed the promising potential of the computational model of skin growth. Tepole *et al.* [57] later extended this model by considering skin as an eight-chain transversely isotropic material [14]. Computational relaxation and creep tests were conducted to study the evolution of in-plane area stretch. Skin growth due to the application of circular-, square-, rectangular- and crescent-shape tissue expanders was also simulated and confirmed that such computational tools can assist clinicians in planning and providing quantitative insight into complex surgical procedures. Several iterations of the original Tepole *et al.*'s model [55] were made by the same group, mostly focusing on refining the computational procedures for simulating the inflation of the tissue expander [3, 58, 59]. Tepole *et al.* [60, 61] integrated *in vivo* experiments conducted on pig and isogeometric finite element techniques to calibrate and validate their computational growth simulations.

1.11 Thermomechanics

Thermomechanical phenomena are an essential aspect of skin physiology [62] through the natural functions of the skin such as thermo-regulation but also play a central role in traumatic injury scenarios such as multiple-degree burns induced by high temperature resulting from external heat sources (e.g. fire) or from friction interactions (e.g. deployment of airbag in automotive accidents can create severe burns of the upper body, particularly of the face, by heat-generating rubbing of the airbag membrane against the skin) [63]. The coupling between thermal effects and mechanical loads, and its subsequent effect on the biochemistry of the skin is particularly relevant to the formation of pressure ulcers (also known as pressure sores) and skin blisters [64, 65] where the notion of *skin microclimate* is key [66]. Skin microclimate is embodied by the intimate coupling of temperature and relative humidity at the surface of the skin which affects the microstructure and mechanical properties of the skin, and, can therefore lead to loss of skin mechanical integrity and barrier function. These few examples illustrate why it is relevant to develop advanced mechanistic constitutive models of the skin capable of replicating and predicting the potentially strong interplay between mechanics, thermodynamics and biochemistry.

The need to develop a fundamental understanding of how thermal exchanges across and at the surface of the skin operate is two-fold. At a fundamental level, it is first essential to unveil the complex physiology of skin in health, disease and ageing. From the knowledge bases previously established, one can seek to optimise the design and functionalities of devices intended to interact with the skin whilst ensuring protection of this vital organ. A discussion of these aspects and a review of state-of-the-art models up to 2011 are discussed in the excellent monograph by Xu and Lu [62].

The development of medical therapies involving thermal phenomena such as laser surgery, hyperthermia procedures for cancer treatment, infrared light therapy or cryotherapy has been responsible for driving research efforts toward the formulation of mathematical models of skin thermomechanics [62, 67]. Abnormal and potentially harmful thermomechanical loading of the skin can arise from diverse sources such as those discussed below. Associated with the ever-growing popular practice of skin tattooing as a decorative art form [68], is the subsequent need to have tattoos removed, typically after a few years [69].

Removal procedures are mainly based on the sublimation of ink pigment particles by generation of localised very high temperatures produced by Q-switched lasers [69, 70]. The wavelength of the laser source is tuned to match that of the absorption wave length of the specific colour of a given tattoo pigment. A laser pulse is then emitted for a duration shorter than the thermal relaxation time which represents the time required for a structure to cool down to half of its heating temperature.

However, the immediate and long-term thermal, photochemical and biological effects of such a destructive technique on a living tissue remain unclear. Severe side effects have been observed including dyspigmentation and textural changes because of the role of melanin which may have absorption wave lengths overlapping those of the targeted tattoo pigments. Other consequences of laser treatment include rupture of blood vessels, aerosolisation of tissue (i.e. generation of an instantaneous and localised plasma) and carcinogenicity. Another significant side effect of tattoos is the potential for patients undergoing MRI scanning procedures to sustain burn injuries [71, 72]. The presence of ferromagnetic metallic compounds in tattoo pigments, especially iron oxide, leads to electromagnetic interactions with the magnetic field produced by MRI machines. This effectively generates an electric induction current that heats the skin tissue from the inside. Recent armed conflicts in the Middle-East have highlighted the need to develop efficient soldier clothing and protection equipment that can be optimised to operate in extreme temperature environments [73]. This also apply to space exploration, and is also of particular relevance, considering alarming climate change facts and predictions [74]. Military and law-enforcement forces have also pioneered the use of directed-energy weapons (e.g. Active Denial System developed by the US Air Force Research Laboratory [75]) which rely on high-powered beam of high-frequency waves (95 GHz). Like a traditional microwave oven, these millimeter waves excite water and lipid molecules producing instant intense heat and pain in the skin [76]. As a complementary role to clinical and biological studies, modelling has the potential to shed light on complex multiphysics phenomena involving thermal transfer, operating in a highly compliant multiscale living structure. A brief review of state-of-the-art continuum models of skin thermomechanics post-2011 can be found in [67]. These authors developed the first finite deformation thermomechanical model of the skin that accounts for biological heat sources as proposed by Pennes [77]. Accounting for the finite deformations that the skin can sustain, within a thermomechanical fully coupled constitutive model, is essential for some applications: for example, deformations induced by the application of a thermal treatment device or by the growth of a cancerous tumour growth can be large. Moreover, even in physiological situations, the skin can sustain finite strains. McBride *et al.* [67] implemented their constitutive law into a finite element code and analysed a geometrically idealised four-layer finite element skin model. Although limited by the availability of dedicated experimental data in terms of thermomechanical and geometrical properties for each skin layer, the coupled-physics framework enjoys a sound thermodynamically consistent formulation that could be experimentally validated in the future.

1.12 Skin microrelief

Skin microrelief is made of a network of furrows and ridges—also called *sulcus cutis* or glyphic patterns—criss-crossing each other and thus delimiting polygonal plateaux with rectangular, square, trapezoidal and triangular shapes. These polygonal patterns—present at birth—lose their isotropic distribution with age and become more anisotropic by forming preferred structural orientations [78-80]. The characteristics of skin microrelief can be classified according to the orientation and depth of featured lines into primary, secondary, tertiary and quaternary lines [78, 79, 81-84].

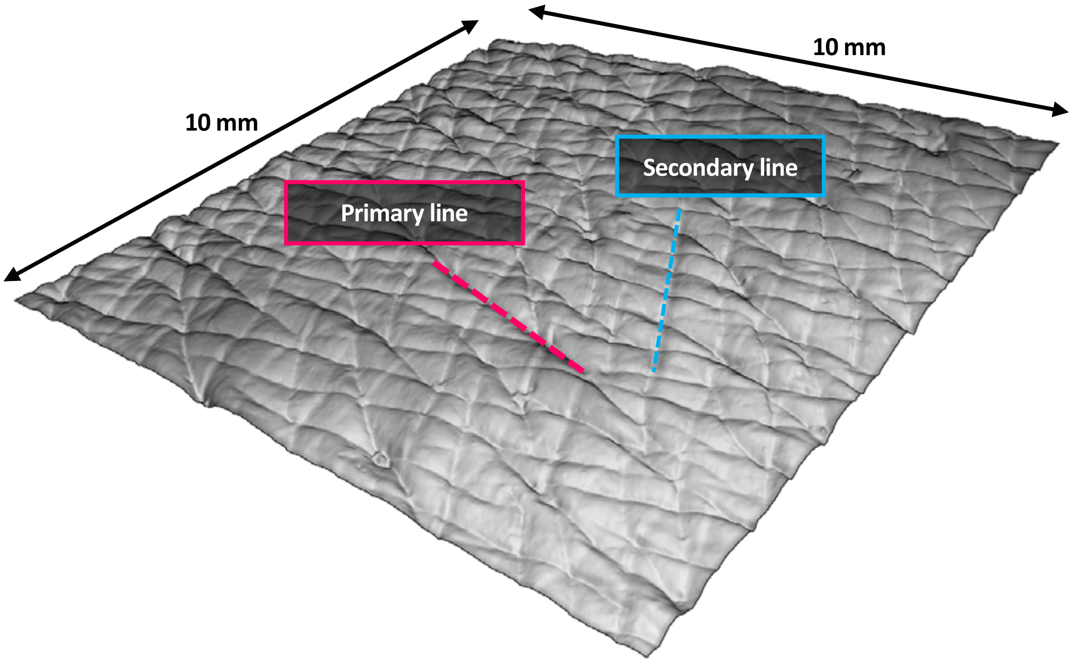

Figure 10. Synthetic image representing the typical microrelief of the skin surface (ridges and furrows), reconstructed from laser scanning profilometry of a silicone replica of a human volar forearm skin patch (40-years old healthy male subject). The acquisition features a 400 x 400 grid of points that was fitted to a NURBS surface.

1.13 Skin wrinkles and the *stratum corneum*

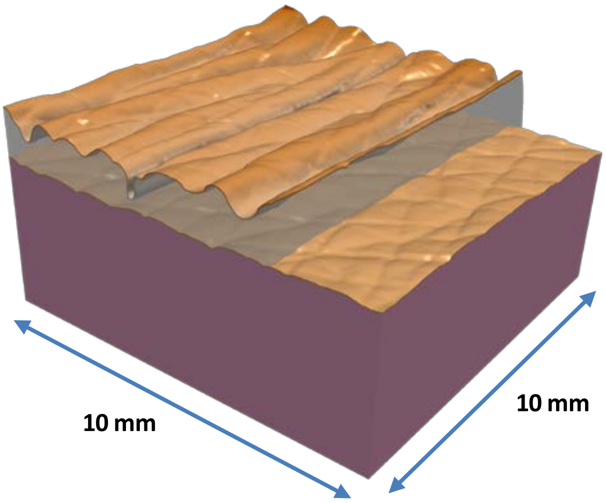

Figure 11. Anatomically-based bi-layer finite element model of human skin featuring a 20 microns-thick *stratum corneum* (top) and a 2.6 mm thick epidermal-dermal substrate, in its undeformed and deformed configurations. In-plane compression of the skin was simulated to trigger wrinkle formation using a robust path-following solving procedure. Young's modulus of the *stratum corneum* is 400 times that of the underlying thicker layer (0.6 MPa). Adapted from Limbert and Kuhl [85].

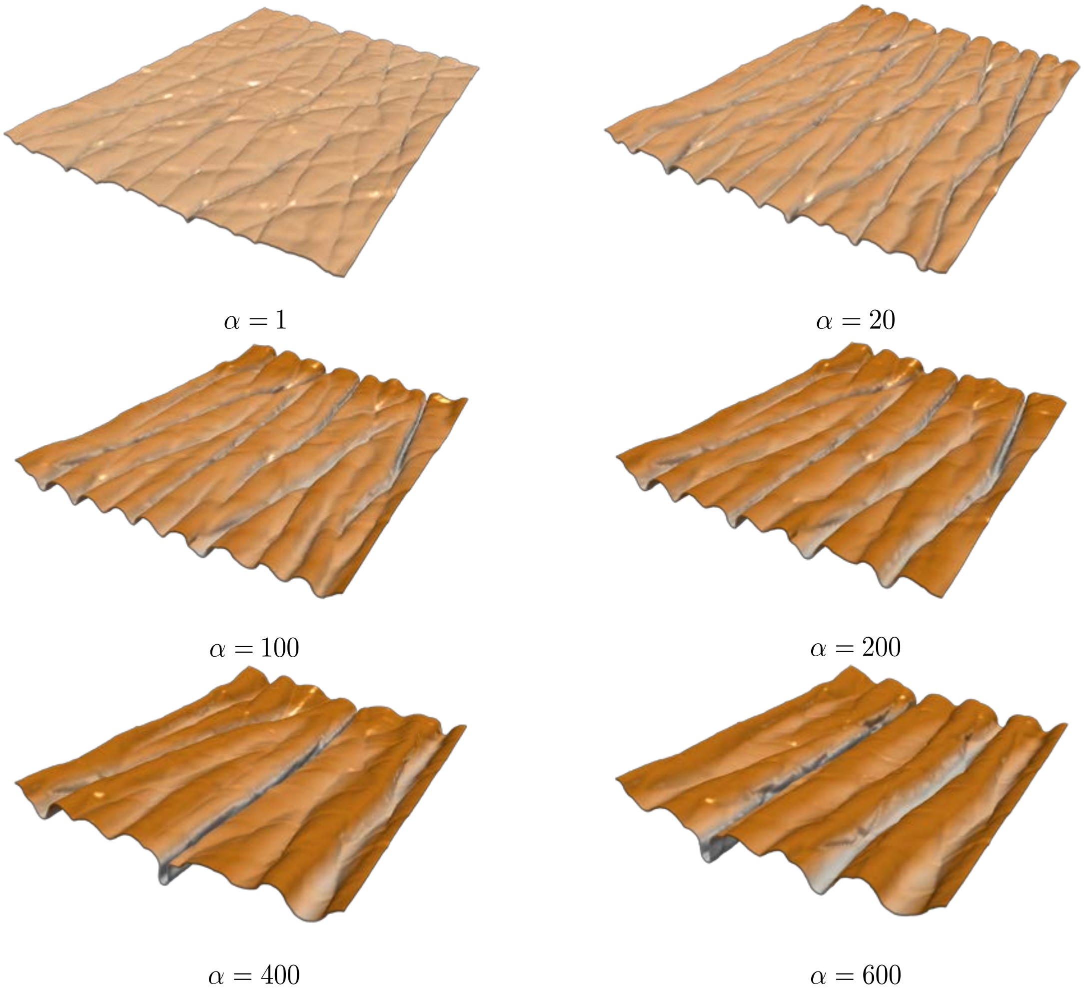

Figure 12. Plot of the deformed stratum corneum layer as a function of the ratio of ground state Young's moduli of the stratum corneum (20 microns-thick) and underlying substrate (0.6 MPa for the substrate) α . Both layers were modelled as neo-Hookean solids and subjected to 25% in-plane compression. This is the same finite element model depicted on **Figure 11**. Adapted from Limbert and Kuhl [85].

2. References

[1] Holzapfel, G.A. 2000 *Nonlinear Solid Mechanics. A Continuum Approach for Engineering*. Chichester, UK, John Wiley & Sons; 470 p.
[2] Belytschko, T., Liu, W.K. & Moran, B. 2000 *Nonlinear Finite Elements for Continua and Structures*. Oxford, Wiley.
[3] Zöllner, A.M., Holland, M.A., Honda, K.S., Gosain, A.K. & Kuhl, E. 2013 Growth on demand: Reviewing the mechanobiology of stretched skin. *J Mech Behav Biomed Mater* **28**, 495-509.
[4] Curnier, A., He, Q.-C. & Zysset, P. 1994 Conewise linear elastic materials. *J Elast* **37**, 1-38.
[5] Holzapfel, G.A. & Ogden, R.W. 2016 On fiber dispersion models: exclusion of compressed fibers and spurious model comparisons. *J Elast*, 1-20.
[6] Lanir, Y. 1983 Constitutive equations for fibrous connective tissues. *J Biomech* **16**, 1-22.
[7] Gasser, T.C., Ogden, R.W. & Holzapfel, G.A. 2006 Hyperelastic modelling of arterial layers with distributed collagen fibre orientations. *J Roy Soc Inter* **3**, 15-35.
[8] Alastrué, V., Martínez, M.A., Doblaré, M. & Menzel, A. 2009 Anisotropic micro-sphere-based finite elasticity applied to blood vessel modelling. *J Mech Phys Solids* **57**, 178-203.
[9] Holzapfel, G.A., Niestrawska, J.A., Ogden, R.W., Reinisch, A.J. & Schriefl, A.J. 2015 Modelling non-symmetric collagen fibre dispersion in arterial walls. *J Roy Soc Inter* **12**.
[10] Sáez, P., Alastrué, V., Peña, E., Doblaré, M. & Martínez, M.A. 2012 Anisotropic microsphere-based approach to damage in soft fibered tissue. *Biomech Model Mechanobiol* **11**, 595-608.
[11] Ogden, R.W. 2016 Nonlinear continuum mechanics and modelling the elasticity of soft biological tissues with a focus on artery walls. In *Lecture Notes from the Summer School "Biomechanics: trends in Modeling and Simulation", September, 2014, Graz, Austria* (ed. G.A.a.O. Holzapfel, R. W.). Heidelber, Springer.
[12] Winitzki, S. 2003 Uniform Approximations for Transcendental Functions. In *Computational Science and Its Applications — ICCSA 2003: International Conference Montreal, Canada, May 18–21, 2003 Proceedings, Part I* (eds. V. Kumar, M.L. Gavrilova, C.J.K. Tan & P. L'Ecuyer), pp. 780-789. Berlin, Heidelberg, Springer Berlin Heidelberg.
[13] Flory, P.J. 1969 *Statistical mechanics of chain molecules*. Chichester-New York, John Wiley & Sons.
[14] Kuhl, E., Garikipati, K., Arruda, E. & Grosh, K. 2005 Remodeling of biological tissue: Mechanically induced reorientation of a transversely isotropic chain network. *J Mech Phys Solids* **53**, 1552-1573.
[15] Kratky, O. & Porod, G. 1949 Röntgenuntersuchungen gelöster Fadenmoleküle. *Rec Trav Chim Pays-Bas Belg* **68**, 1106-1122.
[16] Bischoff, J.E., Arruda, E.A. & Grosh, K. 2002 A microstructurally based orthotropic hyperelastic constitutive law. *J Appl Mech* **69**, 570-579.
[17] Bischoff, J.E., Arruda, E.M. & Grosh, K. 2004 A rheological network model for the continuum anisotropic and viscoelastic behavior of soft tissue. *Biomech Model Mechanobiol* **3**, 56-65.
[18] Garikipati, K., Arruda, E.M., Grosh, K., Narayanan, H. & Calve, S. 2004 A continuum treatment of growth in biological tissue: the coupling of mass transport and mechanics. *J Mech Phys Solids* **52**, 1595-1625.
[19] Flynn, C. & McCormack, B.A.O. 2008 A simplified model of scar contraction. *J Biomech* **41**, 1582-1589.
[20] Flynn, C.O. & McCormack, B.A.O. 2009 A three-layer model of skin and its application in simulating wrinkling. *Comput Meth Biomech Biomed Eng* **12**, 125-134.
[21] Kuhl, E. & Holzapfel, G.A. 2007 A continuum model for remodeling in living structures. *J Mater Sci* **42**, 8811-8823.
[22] Kuhn, W. 1936 Beziehungen zwischen Molekühlgrösse, statistischer Molekülgestalt und elastischen Eigenschaften hochpolymerer Stoffe. *Kolloid-Zeitschrift,* **76**, 258-271.
[23] Arruda, E.M. & Boyce, M.C. 1993 A three-dimensional constitutive model for the large stretch behavior of rubber elastic-materials. *J Mech Phys Solids* **41**, 389-412.
[24] Cohen, A. 1991 A Padé approximant to the inverse Langevin function. *Rheol. Acta* **30**, 270-273.
[25] Nguessong, A.N., Beda, T. & Peyraut, F. 2014 A new based error approach to approximate the inverse langevin function. *Rheol. Acta* **53**, 585-591.
[26] Jedynak, R. 2015 Approximation of the inverse Langevin function revisited. *Rheol. Acta* **54**, 29-39.
[27] Marchi, B.C. & Arruda, E.M. 2015 An error-minimizing approach to inverse Langevin approximations. *Rheol. Acta* **54**, 887-902.
[28] Darabi, E. & Itskov, M. 2015 A simple and accurate approximation of the inverse Langevin function. *Rheol. Acta* **54**, 455-459.
[29] Flynn, C., Rubin, M.B. & Nielsen, P. 2011 A model for the anisotropic response of fibrous soft tissues using six discrete fibre bundles. *Int J Numer Meth Bio* **27**, 1793-1811.

[30] Limbert, G. 2011 A mesostructurally-based anisotropic continuum model for biological soft tissues--Decoupled invariant formulation. *J Mech Behav Biomed Mater* **4**, 1637-1657.

[31] Bischoff, J.E., Arruda, E.M. & Grosh, K. 2002 Finite element simulations of orthotropic hyperelasticity. *Finite Elem. Anal. Des.* **38**, 983-998.

[32] Lanir, Y. & Fung, Y.C. 1974 Two-Dimensional Mechanical Properties of Rabbit Skin—II: Experimental Results. *J Biomech* **7**, 171-182.

[33] Fung, Y.C. 1981 *Biomechanics: mechanical properties of living tissues*. New York, Springer-Verlag.

[34] Muñoz, M.J., Bea, J.A., Rodríguez, J.F., Ochoa, I., Grasa, J., Pérez del Palomar, A., Zaragoza, P., Osta, R. & Doblaré, M. 2008 An experimental study of the mouse skin behaviour: Damage and inelastic aspects. *J Biomech* **41**, 93-99.

[35] Edsberg, L.E., Mates, R.E., Baier, R.E. & Lauren, M. 1999 Mechanical characteristics of human skin subjected to static versus cyclic normal presures. *J. Rehabil. Res. Dev.* **36**.

[36] Ehret, A.E. & Itskov, M. 2009 Modeling of anisotropic softening phenomena: Application to soft biological tissues. *International Journal of Plasticity* **25**, 901-919.

[37] Ehret, A.E., Hollenstein, M., Mazza, E. & Itskov, M. 2011 Porcine dermis in uniaxial cyclic loading: sample preparation, experimental results and modeling. *Journal of Mechanics of Materials and Structures* **6**, 1125-1135.

[38] Li, W. & Luo, X.Y. 2016 An invariant-based damage model for human and animal skins. *Ann Biomed Eng* **44**, 3109-3122.

[39] Volokh, K.Y. 2007 Prediciton of arterial failure based on a microstructural bi-layer fiber-matrix model with softening. *Proceeding of the Amse Summer Bioengineering Conference - 2007*, 129-130
1075.

[40] Volokh, K.Y. 2011 Modeling failure of soft anisotropic materials with application to arteries. *J Mech Behav Biomed Mater* **4**, 1582-1594.

[41] Volokh, K.Y. 2014 On irreversibility and dissipation in hyperelasticity with softening. *Journal of Applied Mechanics, Transactions ASME* **81**.

[42] Yang, W., Sherman, V.R., Gludovatz, B., Schaible, E., Stewart, P., Ritchie, R.O. & Meyers, M.A. 2015 On the tear resistance of skin. *Nat Commun* **6**, 6649.

[43] Mazza, E., Papes, O., Rubin, M.B., Bodner, S.R. & Binur, N.S. 2005 Nonlinear elastic-viscoplastic constitutive equations for aging facial tissues. *Biomech Model Mechanobiol* **4**, 178-189.

[44] Mazza, E., Papes, O., Rubin, M.B., Bodner, S.R. & Binur, N.S. 2007 Simulation of the aging face. *J Biomech Eng* **129**, 619-623.

[45] Rubin, M.B. & Bodner, S.R. 2002 A three-dimensional nonlinear model for dissipative response of soft tissue. *Int J Solids Struct* **39**, 5081-5099.

[46] Weickenmeier, J. & Jabareen, M. 2014 Elastic–viscoplastic modeling of soft biological tissues using a mixed finite element formulation based on the relative deformation gradient. *Int J Numer Meth Bio* **30**, 1238-1262.

[47] Weickenmeier, J., Jabareen, M. & Mazza, E. 2015 Suction based mechanical characterization of superficial facial soft tissues. *J Biomech* **48**, 4279-4286.

[48] Taber, L.A. 1995 Biomechanics of growth, remodeling and morphogenesis. *Applied Mechanics Review* **48**, 487-545.

[49] Epstein, M. 2015 Mathematical characterization and identification of remodeling, growth, aging and morphogenesis. *J Mech Phys Solids* **84**, 72-84.

[50] Neumann, C.G. 1959 The expansion of an arrea of skin by progressive distension of a subcutaneous balloon; us eo fthe method for securing skin for subtotal reconstruction of the ear. *Plastic and Reconstructive Surgery* **19**, 124-130.

[51] Socci, L., Pennati, G., Gervaso, F. & Vena, P. 2007 An axisymmetric computational model of skin expansion and growth. *Biomech Model Mechanobiol* **6**, 177-188.

[52] Rodriguez, E.K., Hoger, A. & McCulloch, A.D. 1994 Stress-dependent finite growth in soft elastic tissues. *J Biomech* **27**, 455-467.

[53] Lubarda, V.A. & Hoger, A. 2002 On the mechanics of solids with a growing mass. *Int J Solids Struct* **39**, 4627-4664.

[54] Menzel, A. & Kuhl, E. 2012 Frontiers in growth and remodeling. *Mech Res Commun* **42**, 1-14.

[55] Buganza Tepole, A., Ploch, C.J., Wong, J., Gosain, A.K. & Kuhl, E. 2011 Growing skin: A computational model for skin expansion in reconstructive surgery. *J Mech Phys Solids* **59**, 2177-2190.

[56] Kuhl, E. & Steinmann, P. 2003 Theory and numerics of geometrically non-linear open system mechanics. *Int J Numer Meth Eng* **58**, 1593-1615.

[57] Buganza Tepole, A., Gosain, A.K. & Kuhl, E. 2012 Stretching skin: The physiological limit and beyond. *Int. J. Non-Linear Mech.* **47**, 938-949.

[58] Zöllner, A., Buganza Tepole, A., Gosain, A.K. & Kuhl, E. 2012 Growing skin: tissue expansion in pediatric forehead reconstruction. *Biomech Model Mechanobiol* **11**, 855-867.

[59] Zöllner, A.M., Buganza Tepole, A. & Kuhl, E. 2012 On the biomechanics and mechanobiology of growing skin. *J Theor Biol* **297**, 166-175.

[60] Buganza-Tepole, A., Gart, M., Purnell, C., Gosain, A. & Kuhl, E. 2015 Multi-view stereo analysis reveals anisotropy of prestrain, deformation, and growth in living skin. *Biomech Model Mechanobiol* **14**, 1007-1019.

[61] Buganza Tepole, A., Gart, M., Gosain, A.K. & Kuhl, E. 2014 Characterization of living skin using multi-view stereo and isogeometric analysis. *Acta Biomater* **10**, 4822-4831.

[62] Xu, F. & Lu, T. 2011 *Introduction to Skin Biothermomechanics and Thermal Pain.* Heidelberg Dordrecht London New York, Springer; 414 p.

[63] Ulrich, D., Noah, E.-M., Fuchs, P. & Pallua, N. 2001 Burn injuries caused by air bag deployment. *Burns* **27**, 196-199.

[64] Sulzberger, M.B., Cortese, T.A., Fishman, L. & Wiley, H.S. 1966 Studies on blisters produced by friction. I. Results of linear rubbing and twisting technics. *J Invest Dermatol* **47**, 456-465 contd.

[65] Knapik, J.J., Reynolds, K.L., Duplantis, K.L. & Jones, B.H. 1995 Friction blisters. Pathophysiology, prevention and treatment. *Sports Medicine* **20**, 136-147.

[66] Gefen, A. 2011 How do microclimate factors affect the risk for superficial pressure ulcers: A mathematical modeling study. *J Tissue Viability* **20**, 81-88.

[67] McBride, A., Bargmann, S., Pond, D. & Limbert, G. 2016 Thermoelastic modelling of the skin at finite deformations. *Journal of Thermal Biology* **62**, 201-209.

[68] Khunger, N., Molpariya, A. & Khunger, A. 2015 Complications of tattoos and tattoo removal: stop and think before you ink. *Journal of Cutaneous and Aesthetic Surgery* **8**, 30-36.

[69] Kuperman-Beade, M., Levine, V.J. & Ashinoff, R. 2001 Laser removal of tattoos. *American Journal of Clinical Dermatology* **2**, 21-25.

[70] Choudhary, S., Elsaie, M.L., Leiva, A. & Nouri, K. 2010 Lasers for tattoo removal: a review. *Lasers in Medical Science* **25**, 619-627.

[71] Ross, J.R. & Matava, M.J. 2011 Tattoo-induced skin "burn" during magnetic resonance imaging in a professional football player: a case report. *Sports Health* **3**, 431-434.

[72] Kreidstein, M.L., Giguere, D. & Freiberg, A. 1997 MRI Interaction with Tattoo Pigments: Case Report, Pathophysiology, and Management. *Plastic and Reconstructive Surgery* **99**, 1717-1720.

[73] Kenney, W.L., DeGroot, D.W. & Alexander Holowatz, L. 2004 Extremes of human heat tolerance: life at the precipice of thermoregulatory failure. *Journal of Thermal Biology* **29**, 479-485.

[74] Schar, C. 2016 Climate extremes: The worst heat waves to come. *Nature Clim. Change* **6**, 128-129.

[75] Defense, U.D.o. 2016 Active Denial Technology. (DOE.

[76] Nelson, D.A., Walters, T.J., Ryan, K.L., Emerton, K.B., Hurt, W.D., Ziriax, J.M., Johnson, L.R. & Mason, P.A. 2003 Inter-species extrapolation of skin heating resulting from millimeter wave radiation: modelling and experimental results. *Health Physics* **84**, 608-615.

[77] Pennes, H.H. 1948 Analysis of tissue and arterial blood Temperatures in the resting human forearm. *Journal of Applied Physiology* **1**, 93-122.

[78] Piérard, G.E., Hermanns, J.F. & Lapière, C.H. 1974 Stéréologie de l'interface dermo-épidermique. *Dermatologica* **149**, 266-273.

[79] Piérard-Franchimont, C. & Piérard, G.E. 1987 Assessment of aging and actinic damages by cyanocrylate skin surface strippings. *Am J Dermopathol* **9**, 500-509.

[80] Setaro, M. & Sparavigna, A. 2001 Irregularity skin index (ISI): a tool to evaluate skin surface texture. *Skin Res Technol* **7**, 159-163.

[81] Lévêque, J.L. 1999 EEMCO guidance for the assessment of skin topography. *J Eur Acad Derm Vener* **12**, 103-114.

[82] Lévêque, J.L. & Audoly, B. 2013 Influence of Stratum Corneum on the entire skin mechanical properties, as predicted by a computational skin model. *Skin Res Technol* **19**, 42-46.

[83] Hashimoto, K. 1974 New methods for surface ultrastructure:comparative studies of scanning electron microscopy, transmission electron microscopy and replica method. *International Journal of Dermatology* **13**, 357-381.

[84] Quatresooz, P., Thirion, L., Piérard-Franchimont, C. & Piérard, G.E. 2006 The riddle of genuine skin microrelief and wrinkles. *International Journal of Cosmetic Science* **28**, 389-395.

[85] Limbert, G. & Kuhl, E. 2017 On skin microrelief and the emergence of expression micro-wrinkles. *Soft Matter*, submitted.